Check for updates

ENGINEERING

Muscle coactivation-inspired stiffness-driven control strategy for antagonistic soft robots

Jie Pan†, Tianyu Chen†, Junwei Li, Yifan Wang*

Copyright © 2026 The Authors, some rights reserved; exclusive licensee American Association for the Advancement of Science. No claim to original U.S. Government Works. Distributed under a Creative Commons Attribution NonCommercial License 4.0 (CC BY-NC).

Soft robots excel at safe and adaptive interaction but are often constrained by limited load capacity and manipulation precision. Antagonistic soft actuators offer a promising route to address these challenges by coupling actuation with variable stiffness, inspired by biological systems such as elephant trunks and octopus tentacles. However, existing control strategies largely treat stiffness as a passive mechanical property, whereas those that incorporate stiffness regulation typically rely on analytical models, limiting their deployment in soft robots with difficult-to-model dynamics. Here, we introduce a muscle coactivation-inspired, data-driven control strategy that explicitly integrates motion control with stiffness modulation, enabling precise and robust control without reliance on analytical models or system-specific tuning. The robot requires only minutes of learning from simple motions to acquire diverse functionalities, including grasping, stiffness sensing, liquid pumping, and reconfigurable bridging. By explicitly harnessing stiffness regulation, this work establishes a general and scalable control paradigm that expands the functional scope of antagonistic soft robots beyond passive compliance.

INTRODUCTION

Soft robots have attracted considerable attention due to their inherent flexibility, which enables remarkable adaptability and safety in diverse environments. However, this flexibility often comes at the cost of reduced load-bearing capacity and limited manipulation precision. To address these limitations, researchers have developed antagonistic soft robots (*1*–*4*), where sets of opposing actuators enable both deformation and tunable stiffness, allowing transitioning between soft and rigid states. This advancement has substantially broadened the applications of soft robots, from manipulators (*5*–*7*) and assistive gloves (*8*–*10*) to grippers (*11*–*13*) and bionic fins (*14*–*16*). Moreover, antagonistic actuation empowers robots to navigate complex terrains with enhanced adaptability and then stiffen to support loads upon reaching their destination (*17*). Despite substantial progress in design and functionality, precise motion control remains a critical challenge for these systems. The ability to accurately manipulate objects and maintain precise movement under variable stiffness is essential for fully developing the potential of antagonistic soft robots across a wide range of applications.

Existing antagonistic soft robots primarily rely on two actuation mechanisms: tendon-driven antagonism (*11*, *18*, *19*) and fluid-driven antagonism (*7*, *20*, *21*). In these systems, differential antagonistic inputs enable actuation, while increasing the combined magnitude of these inputs enhances stiffness (*22*). Although stiffness can be modeled as a linear combination of internal antagonistic inputs (*23*–*26*), and predefined models (*17*, *27*) that incorporate stiffness as part of the system state allow for the simultaneous control of position and stiffness, current implementations remain heavily dependent on these predefined models. Moreover, these predefined models require real-time stiffness state measurement and sensing, which poses a notable challenge in real-world applications (*28*). Addressing these limitations is essential for achieving precise manipulation and unlocking the full capabilities of soft antagonistic robotics in complex and dynamic environments.

School of Mechanical and Aerospace Engineering, Nanyang Technological University, 50 Nanyang Avenue, Singapore 639798, Singapore.
*Corresponding author. Email: yifan.wang@ntu.edu.sg
†These authors contributed equally to this work.

To address these challenges, we draw inspiration from biological muscle systems, particularly in human arm movements, and incorporate modern data-driven methodologies. Previous studies have revealed that increased muscle coactivation enhances motion accuracy in human (*29*–*34*). During arm movements, the central nervous system increases limb stiffness when higher spatial accuracy is required, even in the presence of destabilizing forces (*29*). Numerical simulations and experimental studies have further demonstrated that coactivation of antagonistic muscle pairs around joints notably improves the accuracy of reaching movements (*30*, *31*). These findings suggest that the central nervous system uses muscle coactivation as a strategy to increase joint stiffness, thereby enhancing limb stability and movement precision (*32*–*34*). On the basis of these observations, Fig. 1A illustrates an analogy between human neuromuscular control and antagonistic soft robot control using representative tasks such as pouring for the human arm and object grasping for the robot to highlight how stiffness regulation through antagonistic activation can progressively enable more accurate and robust task execution. This bioinspired perspective naturally calls for a control framework that can exploit stiffness regulation without relying on explicit mechanical modeling. The Koopman operator offers a data-driven modeling paradigm that does not rely on predefined system models (*35*–*37*). By lifting the robot's low-dimensional state space into a higher-dimensional Koopman space (*38*, *39*), this approach enables a linear representation of inherently nonlinear systems. When integrated with model predictive control (MPC) (*40*–*42*), which efficiently manages system constraints such as stiffness limitations, this strategy provides a robust solution for precise motion control of antagonistic soft robots.

In this work, we introduce a muscle coactivation-inspired, stiffness-based, data-driven control strategy for antagonistic soft robots, enabling precise motion control and a wide range of versatile applications. We validate this strategy using an antagonistic soft robot featuring a scale-inspired layered structure (*43*) as a case study. To further demonstrate generality, we also validate the proposed control strategy on a tendon-driven antagonistic soft robot. The proposed framework uses a Koopman-based MPC approach to solve optimization problems while incorporating stiffness constraints. The control model leverages decoupled bilinear Koopman dynamics, constructed

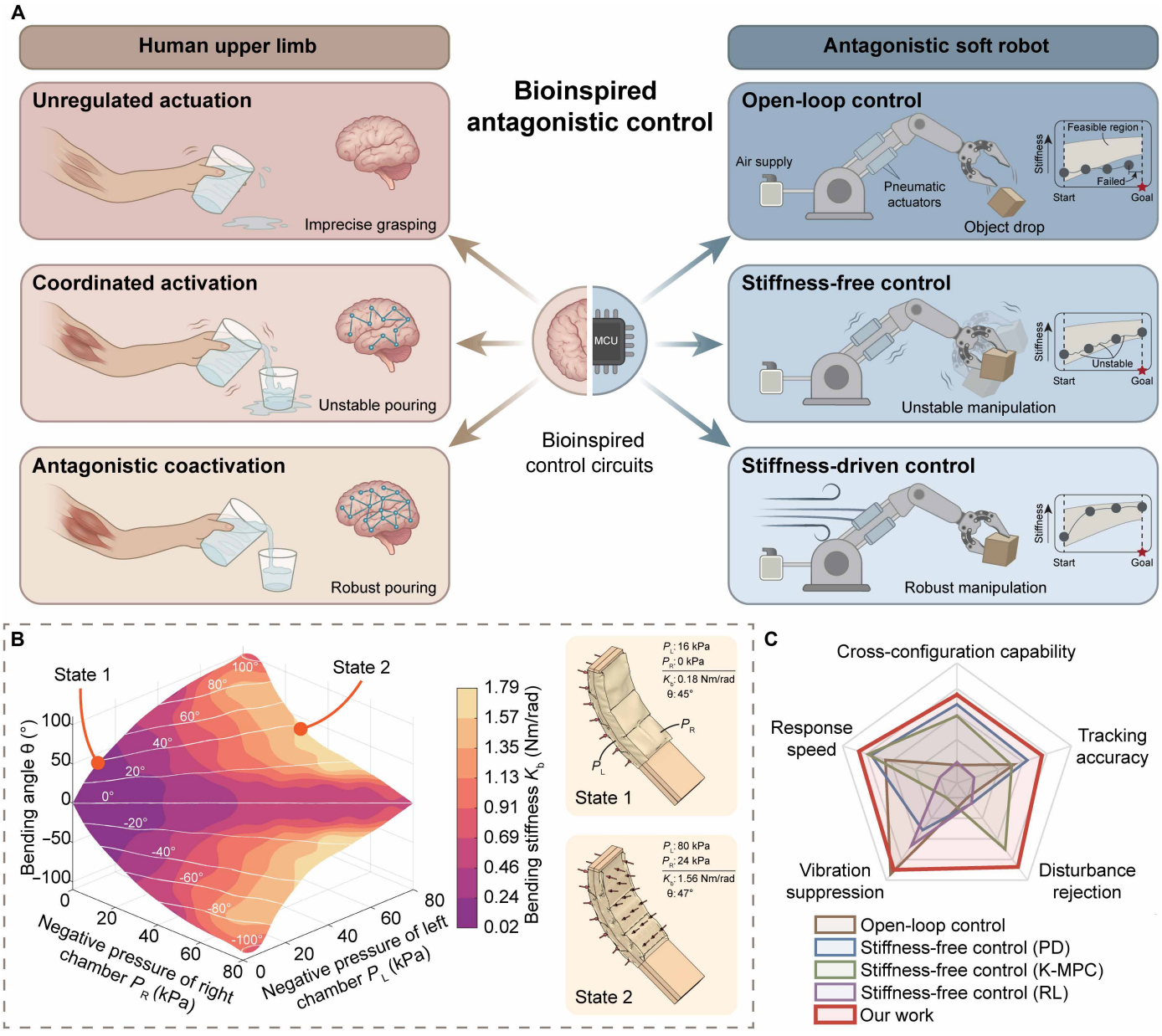


Fig. 1. Bio-inspired stiffness-driven control for antagonistic soft robots. (**A**) Bioinspired antagonistic control: mapping human motor strategies to soft robot control. Left: Using a pouring task as an illustrative example, the human upper limb demonstrates distinct muscle activation and coordination strategies, including unregulated activation without effective control, coordinated activation with limited stability, and antagonistic coactivation enabling stable and precise manipulation. Right: Analogously, the antagonistic soft robot performing an object grasping task implements corresponding control paradigms, including open-loop control, stiffness-free control, and stiffness-driven control. Inspired by biological coactivation, stiffness-driven control regulates antagonistic activation to modulate effective stiffness, resulting in robust and accurate task execution. (**B**) FE simulation results of the robot's performance. The surface plot shows the relationship between negative pressure inputs in both chambers, bending angle θ, and bending stiffness K_b. Color indicates bending stiffness levels, while contour lines represent bending angles. Insets demonstrate how similar bending angles (~45°) can be achieved with different pressure combinations, resulting in varied bending stiffness values. (**C**) Comparisons of tracking accuracy, disturbance rejection, vibration suppression (low deflection), response speed (high deflection), and cross-configuration capability for open-loop control, stiffness-free control, and stiffness-driven control methods. A quantitative description of these performance metrics is provided in note S1.

solely from state-input time series data. Motivated by experimental observations and supported by finite element (FE) analysis (Fig. 1B), we formulate a stiffness constraint to capture stiffness modulation commonly observed in antagonistic soft robots. This constraint does not rely on any explicit mechanical model and eliminates the need for real-time stiffness measurement during robot operation. In addition, we integrate a deep Koopman feedforward compensator to enhance response speed during large deflection motions. This stiffness-driven control strategy demonstrates superior overall performance compared with open-loop control and stiffness-free methods across multiple performance metrics, as illustrated in Fig. 1C. We further validate its efficacy through diverse applications, including

functioning as a soft gripper, stiffness sensor, liquid pump, and reconfigurable bridge. Unlike traditional approaches that rely on targeted and complex modeling (*44*–*46*), our strategy can be applied to antagonistic soft robots exhibiting stiffness-activation coupling without requiring intricate analytical models, highlighting its versatility, robustness, and potential to advance the field of soft robotics.

RESULTS

Design and characterization of the antagonistic soft robot

Antagonistic soft robots typically consist of two opposing actuators, with their functionality relying on the ability to deform by actuating one single side while increasing stiffness through simultaneous activation of both sides. In this study, we create an antagonistic robot based on the scale-inspired layered structure (*43*), as depicted in fig. S1. The robot comprises two back-to-back units of the layered structure, separated by a latex film. Additional latex films envelop the outer sides of both units, forming independent, airtight chambers for actuation. An inertial measurement unit (IMU) is mounted at the end of the robot to record its bending angle. The scale-inspired layered structure consists of a base layer (yellow) and multiple scales (red), both incorporating programmed surface patterns. When negative pressure is applied to either side, the surface patterns engage, causing the robot to morph to a predefined shape while simultaneously increasing stiffness. This robot design is selected due to its dual capability of achieving controlled deformation and stiffness variation simultaneously.

A common limitation of single-channel soft actuators is the coupling of deformation and stiffness. Antagonistic design addresses this constraint, enabling independent modulation of both deformation and stiffness. To evaluate the shape-morphing and stiffness variation capabilities of the antagonistic robot, we conducted FE simulations to characterize its deformation and stiffness under various negative pressure inputs (0 to 80 kPa) applied to both chambers (see Materials and Methods for simulation details). The negative pressures applied to the left and right chambers are denoted as P_L and P_R, respectively. The results, summarized in Fig. 1B, show the bending angle θ of the robot as a surface, with the colored heatmap indicating the corresponding bending stiffness K_b. The simulations reveal that the antagonistic robot achieves an 88-fold increase in bending stiffness, ranging from 0.02 to 1.79 Nm/rad. These results confirm the decoupling of deformation and stiffness in our design. To further illustrate this capability, we highlight two representative actuation states shown in the insets of Fig. 1B, both achieving a similar bending angle of ~45°. State 1 corresponds to single-side actuation, where only the left chamber is depressurized (16 kPa in the left chamber and 0 kPa in the right chamber), resulting in a stiffness of 0.18 Nm/rad. In contrast, state 2 uses dual-side actuation, with higher negative pressures in both chambers (80 kPa in the left chamber and 24 kPa in the right chamber), yielding a much higher stiffness of 1.56 Nm/rad. Despite similar postures, these two configurations demonstrate considerably different stiffness values, validating the robot's ability to actively modulate stiffness at a given deformation. In addition, the white contour lines in Fig. 1B highlight that, at a fixed bending angle, the robot's stiffness increases monotonically with the sum of negative pressures in both chambers.

This ability to achieve the same bending angle with different stiffness levels is a fundamental characteristic of antagonistic soft robots with variable stiffness. However, this feature also introduces control challenges common to antagonistic soft robots, as it increases motion uncertainty. In addition, the pneumatic actuation typically results in notable system delays, which can hinder responsive operation. Precise control at small angles presents another difficulty, as it requires highly fine-tuned input adjustments. These challenges underscore the need for an advanced control strategy that not only addresses the inherent complexities of antagonistic soft robots but also fully capitalizes on their potential for versatile and precise operation.

Stiffness-based data-driven controller design

Our data-driven control strategy for antagonistic soft robots is illustrated in Fig. 2A and detailed in Materials and Methods. The process begins with collecting robot state data under various input series. These data are then used to construct Koopman dynamics, which provides a linear representation of the robot's behavior by mapping the low-dimensional state space to a higher-dimensional Koopman space. This Koopman framework facilitates both state prediction (Fig. 2B) and controller design. The stiffness-based data-driven controller incorporates two key innovations. First, a feedforward compensator is introduced to enhance response speed during large deflections. This compensator predicts expected inputs based on target states and amplifies the inputs in high-deflection scenarios to mitigate motion uncertainty. Second, a decoupled bilinear lifting model expands the Koopman space by lifting each state-input series from the state space to the Koopman space, generating a lifting state. The lifting state, combined with Koopman dynamics, is then used in a stiffness-driven solver to optimize input sequences. The solver includes a penalty term for the sum of inputs, reflecting the relationship between increased inputs and enhanced stiffness. Last, through continuous interaction between the robot's state and the controller, the system achieves precise motion control. This comprehensive approach highlights the potential of our strategy to expand the capabilities of antagonistic soft robots across diverse applications.

To quantitatively evaluate the performance of the proposed strategy, we conducted real-time path-tracking experiments using the antagonistic soft robot. The experimental setup is depicted in Fig. 2C. The input signal consisted of the duty cycles of the pulse width modulation (PWM), which were proportional to the negative pressures applied to each chamber of the robot.

The experimental results are shown in Fig. 2D and fig. S2. The experiment included a three-stage path-tracking test: low deflection, medium deflection, and high deflection. Our approach was compared with three other control strategies: proportional-derivative (PD), Koopman-based MPC (K-MPC), and reinforcement learning (RL) without stiffness considerations. Implementation details of the RL controller are provided in note S2. In the low-deflection scenario, PD, K-MPC, and RL all exhibit noticeable chattering, with average angular velocities of 2.09°, 3.45°, and 1.44°/s, respectively. In contrast, our method achieves smoother motion with an average angular velocity of 0.43°/s. Moreover, the average sum of inputs for PD, K-MPC, RL, and our method are 1.41, 15.52, 45.45, and 157.22%, respectively. A higher input sum correlates with increased stiffness in the antagonistic robot. The substantially higher input sum achieved by our method highlights its explicit consideration of stiffness during movement, enabling reduced chattering and improved precision in low-deflection path tracking. These findings demonstrate that incorporating stiffness into the control framework substantially enhances motion quality in soft robotic systems.

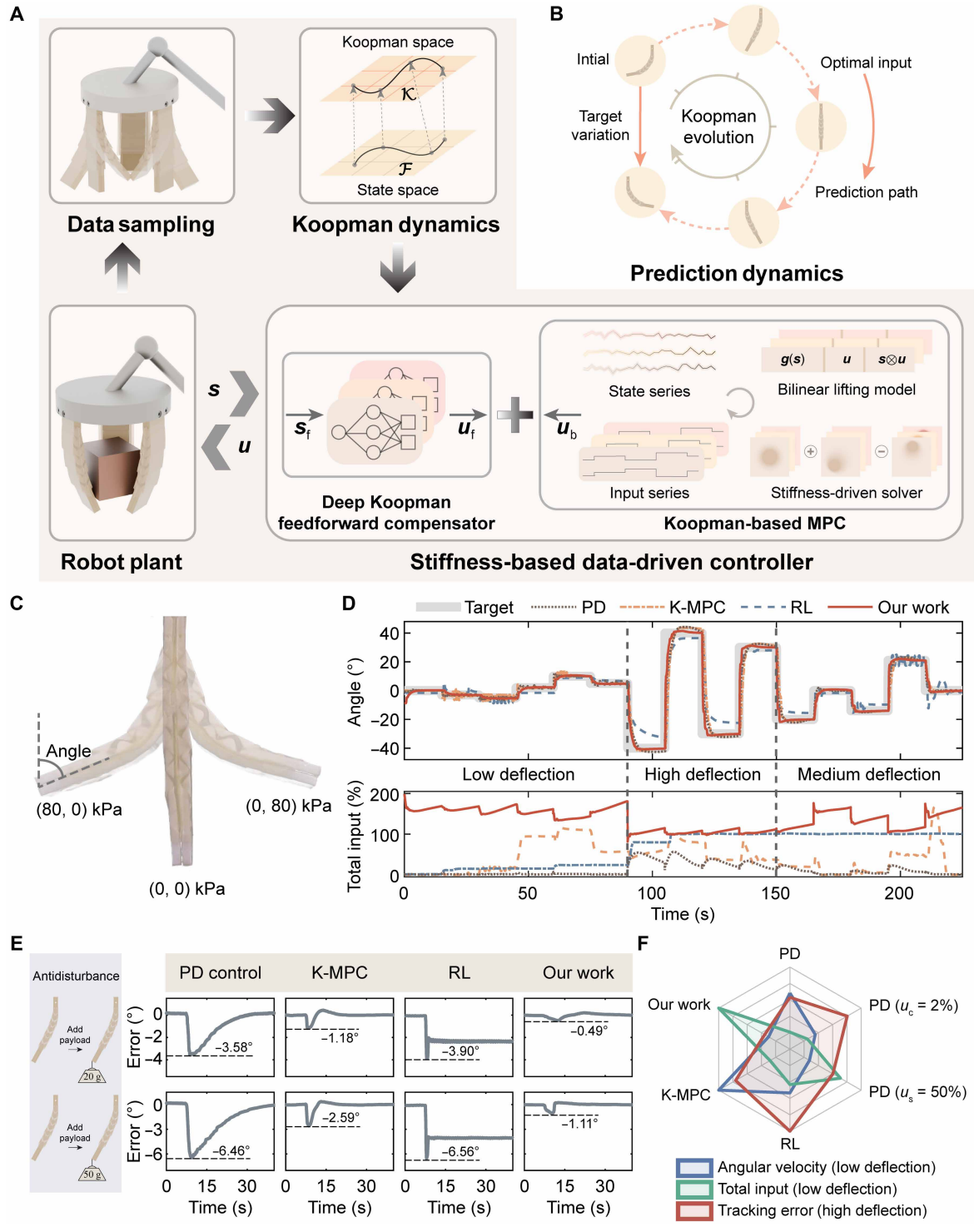


Fig. 2. Data-driven control strategy for antagonistic soft robots: framework and experimental validation. (**A**) Control framework. Data collection of robot state-input pairs is used to learn Koopman dynamics, which enable future state prediction. The predicted states are then exploited by a stiffness-based data-driven controller, incorporating a deep Koopman feedforward compensator, a bilinear lifting model, and a stiffness-driven solver. The controller operates in a closed loop with the robot to accomplish various tasks. (**B**) Koopman-based state prediction. The learned Koopman model is used to predict future robot states for control. (**C**) Experimental setup. (**D**) Real-time path tracking experiments. Tracking performance comparison among the proposed method, PD control, Koopman-based MPC, and RL-based controller. (**E**) Antidisturbance test. Tracking performance under external loads of 20 and 50 g while maintaining the bending angle at 20°. (**F**) Comparisons of the angular velocity (indicating chattering), the sum of inputs (reflecting stiffness), and the tracking error between our work and others. The results are normalized by the maximum value of each metric.

In the high-deflection scenario, our method demonstrates superior tracking performance and faster response. The average tracking errors for PD, K-MPC, RL, and our method are 5.83°, 7.61°, 10.82°, and 2.96°, respectively. In addition, our method achieves an average response time of 2.09 s, outperforming PD (3.67 s), K-MPC (3.25 s), and RL (12.40 s). Across the entire three-stage path-tracking experiment, the average tracking errors for PD, K-MPC, RL, and our method are 2.37°, 3.21°, 5.25°, and 1.58°, respectively. These results demonstrate the effectiveness of our approach in achieving a balance between fast response and robust performance across various deflection amplitudes. An ablation study, detailed in note S4 and quantitatively summarized in table S3, further clarifies the respective roles of the stiffness constraint and the feedforward compensator. The results indicate that the two modules play complementary roles within the proposed framework.

To assess the robustness of the proposed muscle coactivation-inspired control method, we conducted experiments in which the robot was required to maintain a 20° bending angle under external perturbations. The results before and after attaching payloads of 20 and 50 g are shown in Fig. 2E. The attached payload may cause the robot to respond differently under the same control input, thereby introducing deviation from the nominal input-deformation relationship learned from the training data. Although these load-induced deviations can be partially mitigated by feedback control, PD control, K-MPC, and RL still show noticeable offsets from the target position after the payload is applied. The RL controller, in particular, exhibits persistent offsets under load because the policy is trained offline in a surrogate environment identified under nominal conditions. This suggests that achieving stronger load robustness with RL would likely require a more accurate surrogate environment and richer training data that better capture load-dependent dynamics. In contrast, the proposed framework compensates for load-induced deviations through closed-loop state feedback and online reoptimization while also enhancing resistance to payload-induced deformation through stiffness regulation. As a result, it produces the smallest deviation and tracking error under payload condition. The proposed method also maintains a consistently high sum of inputs before and after the payload is applied, demonstrating the ability of our muscle coactivation-inspired approach to provide enhanced stiffness during motion. An analysis of this load-induced deviation is provided in note S5.

We also conducted additional experiments to investigate heuristic stiffness enhancement, as detailed in note S6, table S4, and fig. S4. In these experiments, we evaluated a fixed-input strategy, in which one actuator was held at a constant input level (1, 2, or 5% PWM duty cycle) while the opposing actuator was controlled by PD and a symmetric preload strategy, in which both actuators were given the same antagonistic preload (10, 20, 50, or 100% PWM duty cycle), and the PD command was applied differentially to generate motion. A detailed definition of the PD controller is provided in Materials and Methods. These results indicate that, although moderate heuristic stiffening can partially improve stability and disturbance rejection, excessive antagonistic input inevitably introduces clear compromises in tracking performance and response speed. In contrast, our approach systematically integrates stiffness regulation into the control framework and, as shown in Fig. 2F, achieves superior overall performance, enabling robust stabilization without substantially sacrificing tracking accuracy across a wide range of motion amplitudes.

Application as a versatile gripper

Soft grippers represent a crucial application of soft robotics, with recent studies highlighting the importance of variable stiffness for handling both soft and rigid objects effectively (*47*–*50*). We therefore applied our proposed control strategy to a soft gripper to demonstrate its effectiveness (Fig. 3). The gripper comprised three antagonistic actuators serving as its fingers, arranged 120° apart. To enhance its functionality, we integrated a perception module into the controller based on input variation (see Materials and Methods for details). This module allows the gripper to sense object interaction through input changes, enabling the completion of various gripping tasks.

To evaluate the effectiveness of our approach in achieving precise motion control, we used the soft gripper to pinch a soft silicone ring (Fig. 3, A and B). The performance of our method was compared against direct actuation without control, where negative pressure was simply applied to one chamber of the robot. Without control, the silicone ring experienced notable deformation under the gripper's force, as illustrated in the upper half of Fig. 3A. In contrast, our method achieved precise pinching with minimal deformation of the silicone ring (lower half of Fig. 3A). As shown in Fig. 3B, the pinching sequence consists of three phases: approach, touch, and grasp, with the grasp phase starting when all three soft arms make contact with the object.

The critical role of stiffness in grasping rigid objects is demonstrated by comparing the performance of our method with PD control (Fig. 3, C and D). During the test, the gripper was first commanded to bend each finger to an angle of 20° without contacting the object. After lifting began at $t = 20$ s, no further input adjustment was made. The gripper was then lifted to perform a power grip on a rigid object (67 g), a method that relies on finger stiffness to lift the object rather than on the compression force against the object. The results show that PD control fails to achieve a power grip, whereas our method succeeds (Fig. 3C). Figure S7 depicts the bending angle of each finger of the gripper and the corresponding input variations. Notably, the input levels in our method are 17, 9, and 22 times higher than those in PD control for the three fingers, respectively. While the gripper is designed to be symmetric, the variations in input levels across the fingers arise from inherent inconsistencies in the manual assembly process of each finger's layered structure.

To further quantify the gripping force, we conducted an experiment using a universal testing machine (Mark-10 Corp) with the gripper attached and the object fixed to the ground. Each finger was bent to a designated angle (15°, 20°, 25°, or 30°) before attempting to grasp and lift the object, while the force-displacement curve was recorded. Our method considerably increases the maximum gripping force compared to PD control: by 391% at 15° bending angle, 177% at 20°, 58% at 25°, and 30% at 30° (Fig. 3E), respectively. These results demonstrate that our method enhances the gripper's stiffness through increased input, thereby unlocking the potential of antagonistic robots as powerful and versatile grippers.

In addition, lightweight delicate objects can be challenging for soft grippers, as positioning variations and manufacturing imperfections may result in asymmetric force application, increasing the risk of the object tipping over during grasping. To further illustrate the proposed method in grasping lightweight delicate objects, we used a cup-shaped object weighing 17 g with a maximum cross-sectional diameter of 64 mm (Fig. 3F). While direct actuation without control was able to lift the object, it resulted in pronounced tipping. In contrast, our method successfully picked up the object

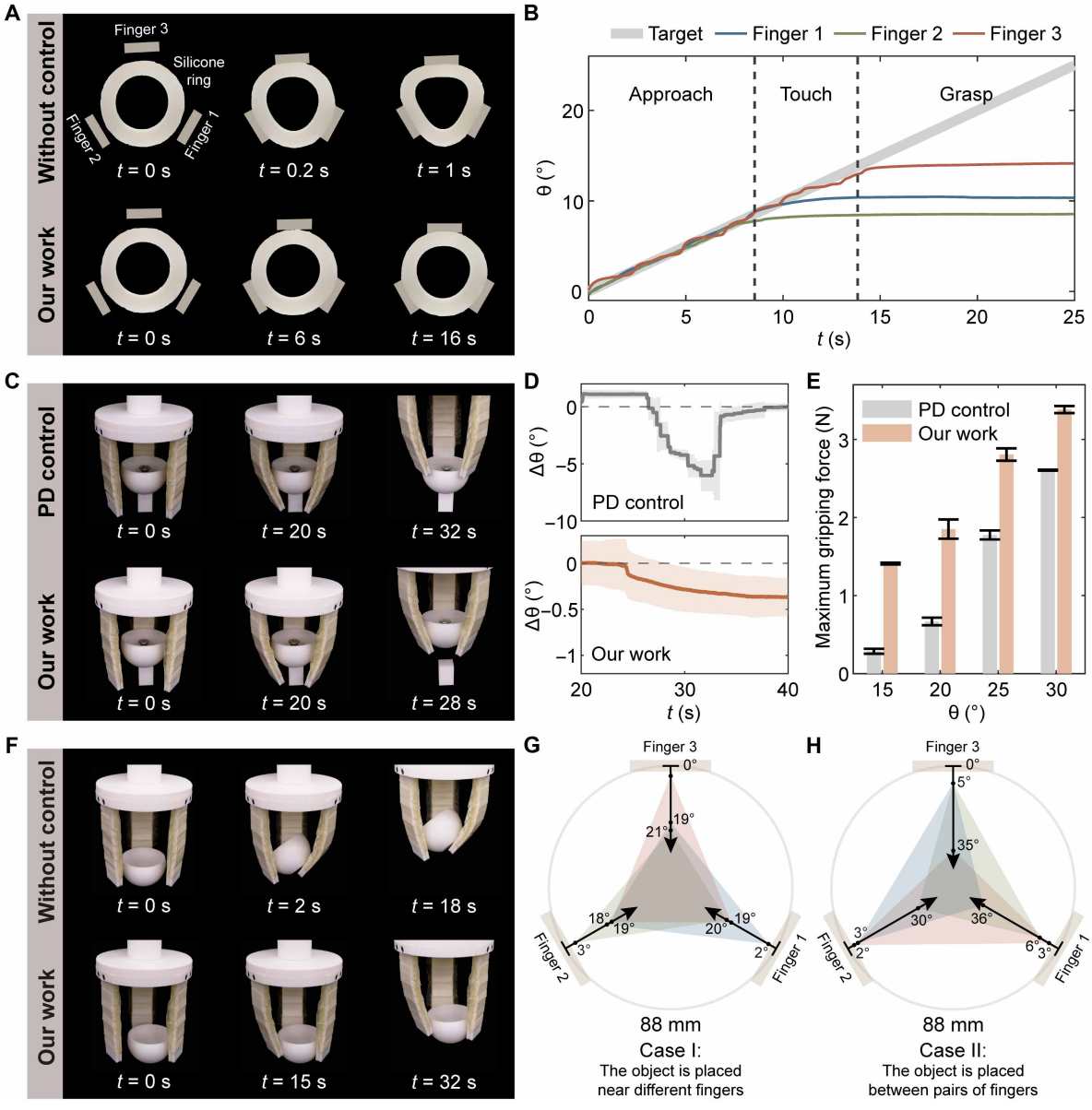


Fig. 3. Grasping performance of the soft gripper enabled by the data-driven control strategy. The gripper consists of three antagonistic robots spaced 120° apart. (**A**) Soft silicone pinching. Comparison between our method and direct actuation without control. (**B**) Angle changes in each finger during the pinching task, where the pinching sequence includes approach, touch, and grasp. (**C**) Rigid object grasping. Comparison between our method and PD control. (**D**) Comparison of the averaged angle tracking error of the three fingers. (**E**) Comparison of the maximum grasping force achieved at different bending angles. (**F**) Handling lightweight objects. Comparison between our method and direct actuation without control. (**G**) Finger bending angles for object placement near individual fingers. (**H**) Finger bending angles for object placement between finger pairs. In both (G) and (H), each triangle represents one of the tested object positions, with its three corners corresponding to the three fingers, and the arrows indicating the direction of finger movement. In (G), yellow, red, and purple triangles indicate placements near finger 1, finger 2, and finger 3, respectively. In (H), the same colors indicate placements near the midpoints between finger 2 and finger 3, finger 1 and finger 3, and finger 1 and finger 2, respectively.

while maintaining it in a flat, stable position, even when the object was placed at the edge of the gripper's reach, farthest from the center (Fig. 3, G and H). This comparison highlights the importance of active control for grasping lightweight delicate objects in a stable and balanced manner. To quantitatively evaluate the performance and robustness of our method, we systematically varied the position of the object, placing it near individual fingers or between pairs of fingers, and measured the resulting grasping angles of each finger, with the tested positioning and grasping configurations shown in fig. S8. The results across various scenarios demonstrate the ability of our method to apply balanced forces, adapting effectively to different object positions.

Because of these advantages, our stiffness-based control strategy enables the gripper to handle a wide variety of objects with varying stiffness, sizes, and shapes, as illustrated in fig. S9. The gripper demonstrates its adaptability by successfully grasping soft items, such as a sponge and a cake, and stiffer objects, including an apple and a ping pong ball. It also maintains stable grasping performance for

relatively smooth-surface objects that are more prone to slipping, including a glass cup and two beakers of different sizes. For larger objects, such as a toolbox, the gripper initially extends outward to increase its effective span before performing the grasp. In addition, the gripper showcases versatility in manipulating hollow objects, such as a transparent box and a polylactic acid (PLA) sculpture, by hooking them from the inside. Detailed shape and weight parameters for all test objects are provided in table S5.

Application as a stiffness sensor

Having established the fundamental principles and performance of our data-driven approach, we now showcase other versatile applications enabled by our stiffness-driven control strategy. One such application is the use of the antagonistic robot as a stiffness sensor. As illustrated in Fig. 4A, the robot was mounted horizontally and used its precise motion control to measure stiffness, facilitating comparisons between various objects, including a silicone ring, a cotton bag, a sponge, and a PLA block. The robot followed a predefined trajectory and then used its perception module to detect contact with an object. Upon contact, it continued its motion and evaluated the stiffness based on its own deformation. We computed the tracking error over the 4 s following contact, where contact was defined as the moment when the input variation reached 0.06%. The resulting value was used to rank the objects by stiffness. On the basis of our measurements, we establish the stiffness ranking in descending order: PLA block, sponge, cotton bag, and silicone ring. This application highlights the versatility of our stiffness-driven control strategy, enabling the robot to function as an effective stiffness sensor capable of distinguishing materials with varying rigidity.

Building on these single-robot observations, we conducted multifinger stiffness sensing experiments during grasping tasks, with objects sorted according to their stiffness (Fig. 4B). In these experiments,

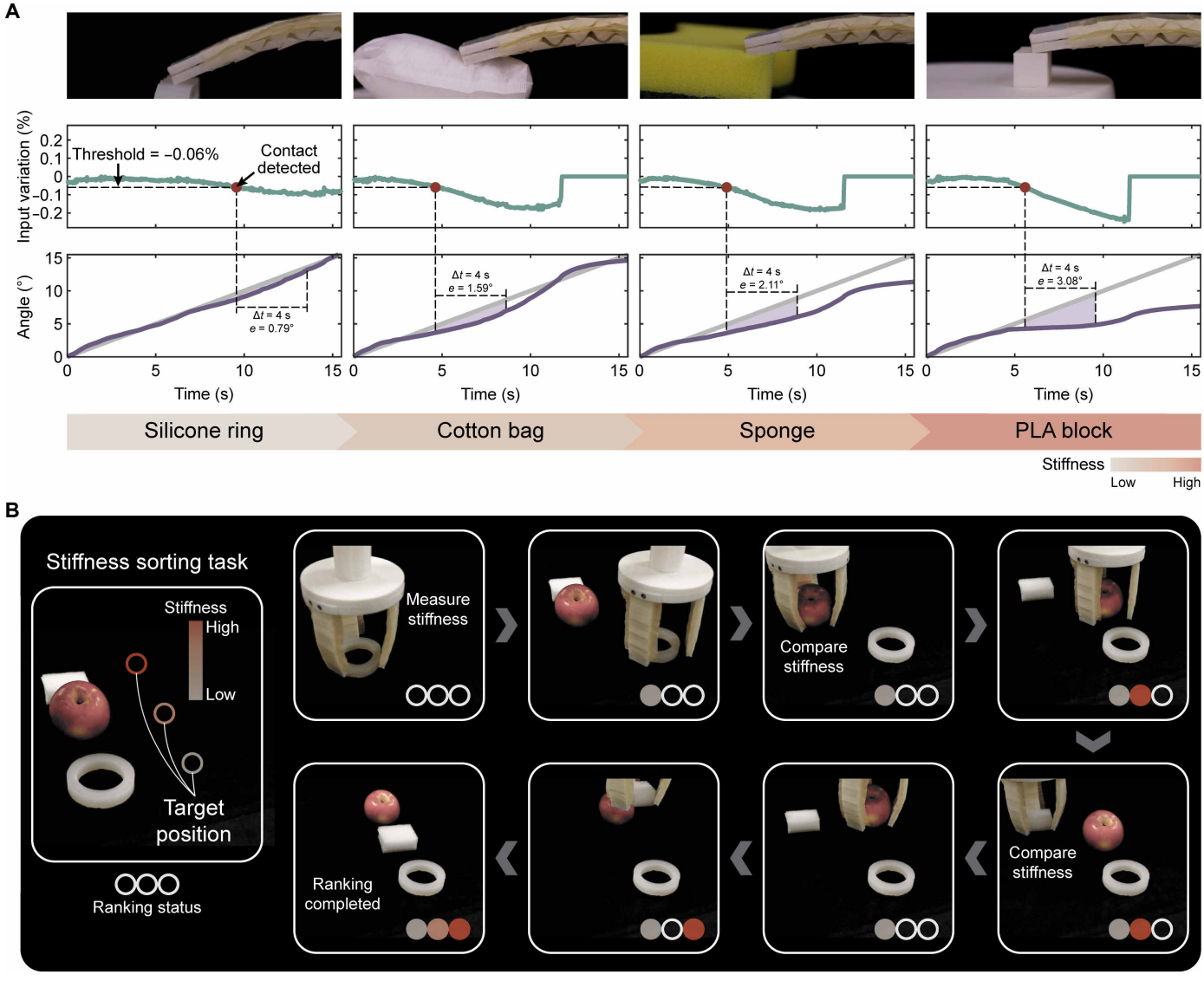


Fig. 4. Stiffness-aware interaction and object sorting. (**A**) Single-finger stiffness sensing. Stiffness is inferred from contact-induced trajectory deviation during predefined motion. (**B**) Stiffness sorting task. A three-finger robotic gripper ranks and sorts objects by stiffness (apple > EPE foam block > silicone ring).

a three-finger gripper mounted on a robotic arm (Dobot CR3) first measured the stiffness of the objects and then grasped and transported them to a target location. The objects included a silicone ring, an expanded polyethylene (EPE) foam block, and an apple. As shown in Fig. 4B, the gripper first measured the stiffness of the silicone ring and placed it at the position representing the lowest stiffness. Next, the gripper measured the stiffness of the apple and compared it with that of the silicone ring, determining that the apple was stiffer. Consequently, the apple was placed at the position representing an intermediate stiffness. The gripper then measured the stiffness of the EPE foam block and found that its stiffness was between that of the silicone ring and the apple. Therefore, the apple was moved to the position representing the highest stiffness, and the EPE foam block was placed at the intermediate stiffness position. Across three trials, the tracking errors for the silicone ring, EPE foam block, and apple are $2.38 \pm 0.07°$, $2.66 \pm 0.05°$, and $3.12 \pm 0.01°$, respectively, confirming that our method enables stiffness-based object ranking during grasping.

Application as a liquid pump

In Fig. 5A, we demonstrated the versatility of our stiffness-driven control strategy by adapting the antagonistic robot to function as a liquid pump. To facilitate liquid transfer, we incorporated a slanted groove along the middle of the robot (see fig. S10B for design details). This configuration, combined with our control strategy, enables the robot to overcome gravity and transport liquid from lower to higher elevations. The pumping cycle operated as follows: First, the robot bent downward to a bending angle of 37° to collect liquid. It then bent upward along a predefined trajectory at a rate of 3°/s until reaching a bending angle of 103° to complete a single liquid transport cycle. Subsequently, the robot bent downward along the same trajectory at an identical rate, preparing for the next cycle (Fig. 5B). By repeating this process, the robot could progressively elevate liquid to higher positions. Our control strategy allowed dynamic adjustment of the collection angle based on the current liquid level, ensuring efficient operation as the source liquid depleted or the target container filled. Without control, the robot would be unable to dynamically adjust the collection angle and liquid flow rate, leading to failures in liquid collection or leakage (Fig. 5C). When the upper-side chamber was driven unilaterally to bend downward, the layered structure of the lower-side chamber could become stuck due to gravity, making it impossible to drive the lower-side chamber to bend upward as intended. This application showcases the potential of our soft robots, supported by the proposed control strategy, in fluid handling and transfer tasks.

Application as a reconfigurable bridge

We further demonstrated the versatility of our control method by applying the stiffness-based data-driven control strategy to a reconfigurable bridge system (Fig. 5D). The bridge consisted of two halves, each powered by an antagonistic robot capable of bending upwards or downwards (see fig. S10C for design details). When both halves are flat, cars can pass over the bridge. When the halves bend upwards, ships can pass underneath. This design allows the bridge to adapt to different traffic needs dynamically.

To accommodate both types of traffic while accounting for gravitational loads, we set the desired bending angle of each half to 95° during the car-passing phase (nearly flat) and 125° during the ship-passing phase (bent upward). Our control strategy enables the bridge to adapt successfully to both car and ship traffic requirements. In contrast, without our approach, the bridge system is prone to malfunction. For instance, during the car-passing phase (Fig. 5Da), applying a negative pressure of 16 kPa to one chamber maintained the bridge in a nearly flat state. However, it resulted in insufficient stiffness, causing the bridge to sink under the car's weight, as illustrated in fig. S11A. In the ship-passing phase (Fig. 5Db), the robots bent upward to 146° and 152° by pressurizing one chamber to a negative pressure of 80 kPa, enabling the ship to pass. However, when the opposite chamber was subsequently driven to the same pressure, the robots failed to return to a flat configuration suitable for car traffic. Instead, the robots only recovered to 119° and 122°, creating an impassable slope, as shown in fig. S11B. This incomplete recovery suggests history-dependent behavior in the soft antagonistic structure, likely due to internal friction between the scales and the base layer (see note S10 for further discussion). The proposed controller does not assume a unique static input-deformation relationship, but compensates for these effects online through closed-loop dynamic control with real-time state feedback. These comparisons underscore the critical role of our stiffness-based data-driven strategy in enabling the soft robotic bridge to adapt to both car and ship traffic while maintaining its structural integrity and functionality.

Generality of the proposed data-driven control strategy

The precise motion control is achieved by dynamically optimizing the robot's stiffness to a high level. Although stiffness cannot be measured directly in real time, we can qualitatively modulate the desired stiffness level by adjusting the sum of antagonistic inputs, as discussed in note S11. This stiffness-aware control principle is independent of a specific actuation modality and thus lends itself naturally to extension across different antagonistic robotic platforms.

To validate the generality of the proposed data-driven control strategy, we further conducted tracking experiments on a tendon-driven antagonistic robotic platform (*51*). The detailed mechanical design and experimental setup are provided in note S12. This platform has a 2-DOF tendon-driven configuration, in which the yaw-pitch motions and tendon tensions are mechanically coupled. Unlike the pneumatic antagonistic robot, whose mechanically independent antagonistic units allow the use of the decoupled bilinear lifting model shown in Fig. 2A, the 2-DOF tendon-driven platform is modeled using a coupled Koopman formulation. Here, the yaw-pitch motion states are modeled together, while the tendon tensions are explicitly included as first-order terms in the lifting function. In this tendon-driven system, stiffness modulation is mainly associated with the sum of tensions in the opposing tendons. Accordingly, the stiffness-related constraint is defined based on the antagonistic tendon tensions.

Figure 6A presents the tracking performance of the tendon-driven antagonistic robot under varying antagonistic force levels (0, 10, and 40 N) and environmental conditions (disturbance-free, with tip-load, and end-effector immersed in silicone oil). The antagonistic force refers to the sum of tension force maintained in the opposing tendons. Higher antagonistic forces correspond to higher stiffness levels. The color indicates the tracking error, with darker shades representing smaller errors. The experimental results indicate that, under disturbance-free conditions, increasing the antagonist force from 0 to 10 N leads to substantial improvements in both tracking accuracy and velocity regulation, whereas further increasing the force to 40 N yields diminishing performance gains. When external payloads are introduced, the motion quality under both 0- and 10-N configurations degrades noticeably, while the 40-N configuration preserves

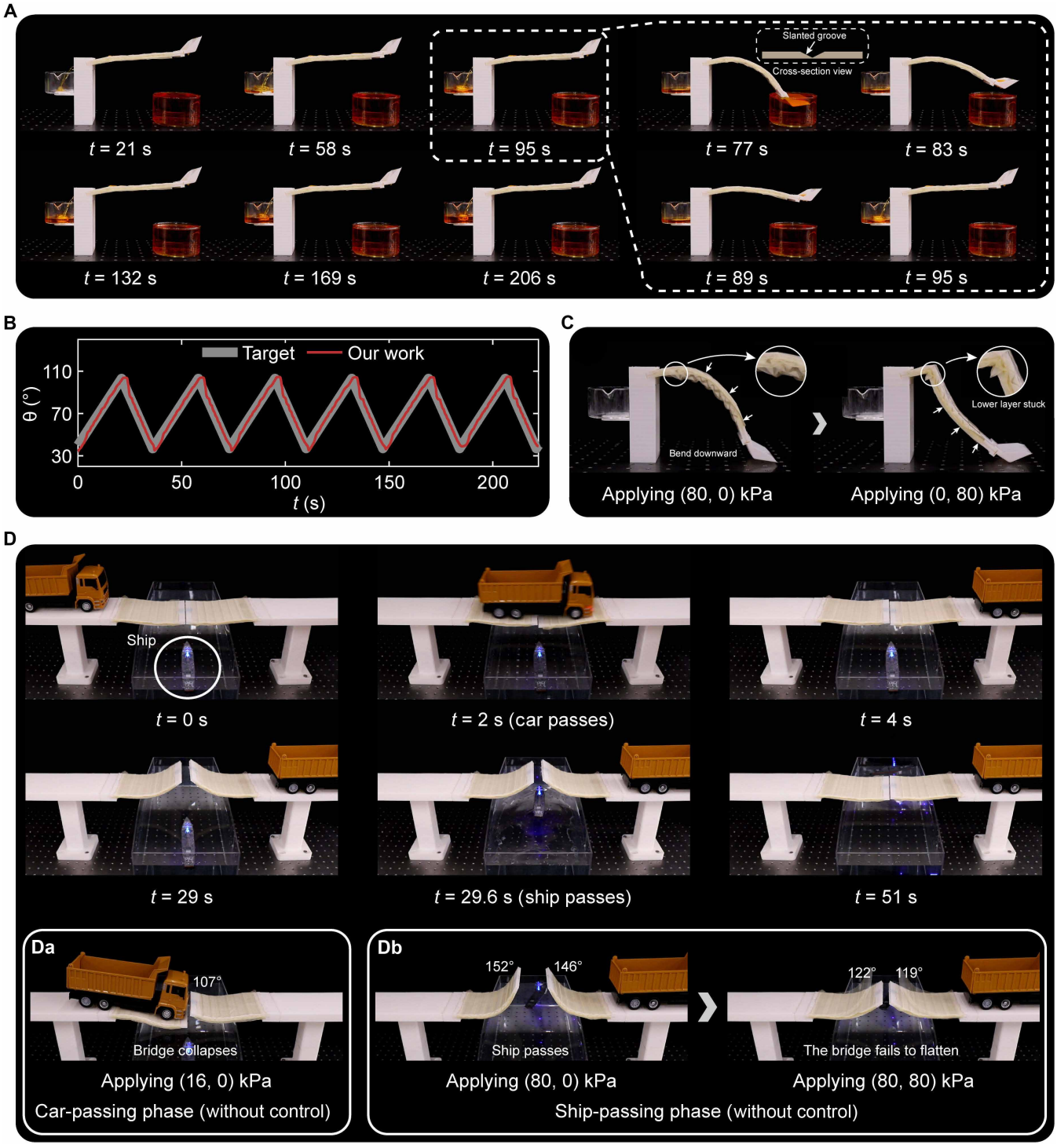


Fig. 5. Versatile applications enabled by the stiffness-based data-driven control strategy. (**A**) Liquid pump. A slanted groove introduced into the robot enables liquid transport against gravity. (**B**) Angle variation of the liquid pump during multiple transfer experiments. (**C**) Failure of the liquid pump without control: Unilateral actuation causes the lower-side chamber to stick under gravity, preventing upward bending. (**D**) Reconfigurable bridge. Two antagonistic soft robots form an adaptive bridge. With our strategy, the bridge accommodates both a 410-g car and ship traffic by adjusting angle and stiffness. Without our control strategy, the bridge fails to function properly. (Da) Car-passing phase without control. The bridge will sink into the water under load. (Db) Ship-passing phase without control. After asymmetric actuation (80, 0) kPa for ship passing, the bridge fails to recover to the horizontal configuration upon reapplying the symmetric input (80, 80) kPa.

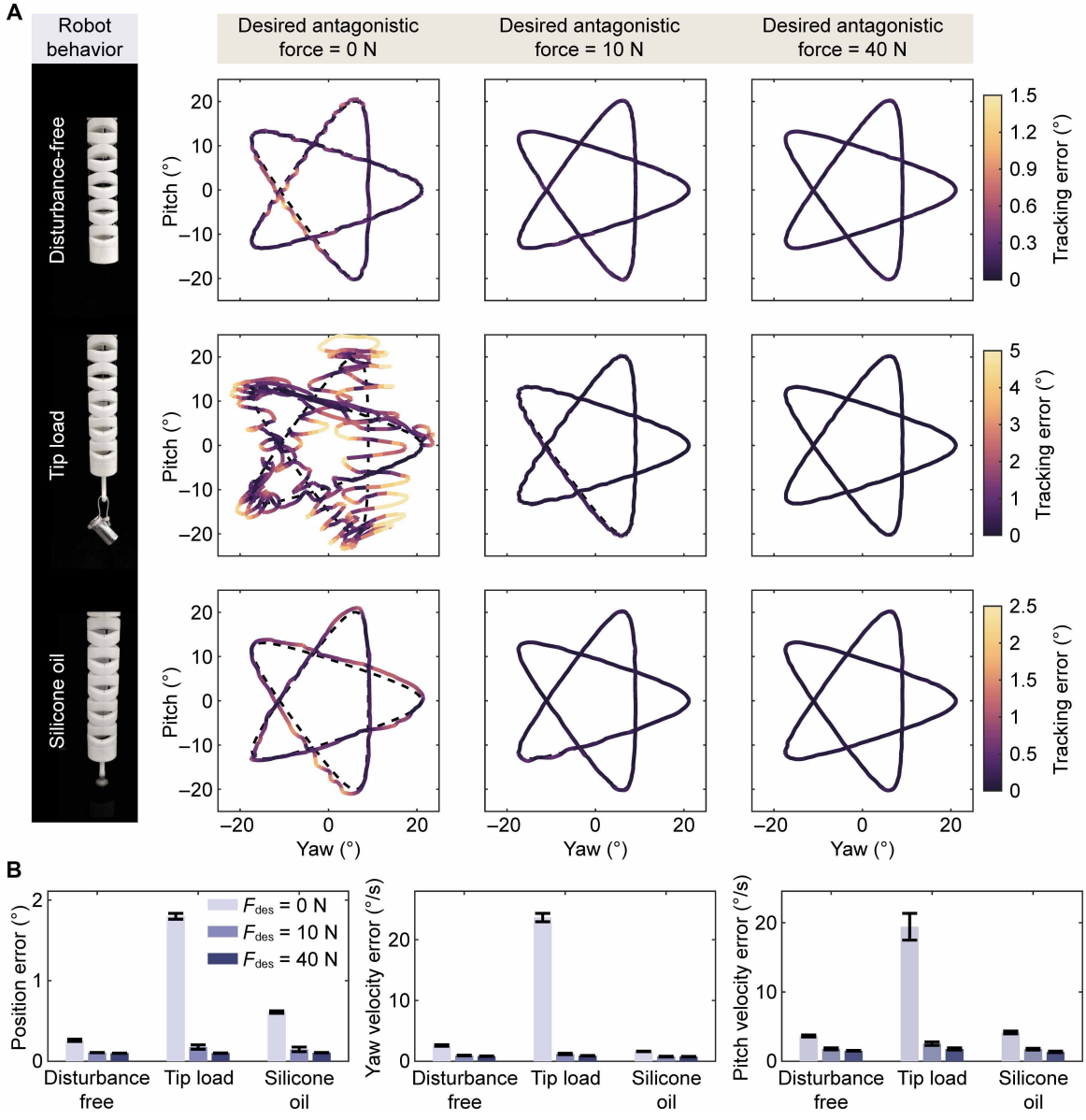


Fig. 6. Generality of the proposed data-driven control strategy. The control framework is extended to a two-degree-of-freedom tendon-driven robot to demonstrate its applicability. (**A**) Tracking performance under varying desired antagonistic forces and environments. Desired antagonistic forces of 0, 10, and 40 N correspond to low, medium, and high stiffness levels, respectively. The environments include disturbance-free, tip-load, and silicone-oil conditions. Color indicates the tracking error. (**B**) Position and angular velocity errors under different antagonistic force levels and environments.

stable and accurate trajectory tracking. These observations suggest that although moderate stiffness levels may be sufficient under less demanding conditions, higher stiffness becomes essential when stronger external disturbances are present. In viscous silicone oil environments, all configurations exhibit reduced velocity errors due to viscous damping effects. However, tracking accuracy at lower antagonist forces (0 and 10 N) deteriorates substantially compared to air, whereas the 40-N configuration consistently maintains superior tracking precision. This further highlights the importance of stiffness modulation in adapting to highly resistive environments. Overall, these results demonstrate that the proposed data-driven control strategy generalizes effectively across antagonistic robotic platforms with different actuation mechanisms by adapting the lifting function and stiffness-related constraint to each platform.

DISCUSSION

In this work, we present a stiffness-based data-driven control strategy for antagonistic soft robots. Our approach draws inspiration from biological muscle systems, where increased muscle coactivation enhances motion precision through greater joint stiffness. Unlike previously reported control methods for antagonistic soft robots (*17*, *25*, *27*, *45*), which generally rely on analytical modeling, explicit stiffness formulations, or platform-specific parameterization, our

work is data-driven and does not require expert knowledge or trial-and-error tuning (see note S3 for a qualitative comparison). It requires only a few minutes of learning from simple movements, enabling high scalability and transferability to various antagonistic variable stiffness soft robots (see table S1 for quantitative comparisons). The consistent performance observed on both pneumatic and tendon-driven antagonistic robots further supports the generality of this stiffness-driven control paradigm.

Beyond the specific control architecture, our experimental results across multiple stiffness levels highlight the critical role of stiffness regulation in antagonistic soft robot control. We observe that variations in antagonistic coactivation substantially affect tracking accuracy, disturbance rejection, and dynamic response, even when the underlying control policy remains unchanged. These findings suggest that stiffness should not be overlooked in controller design for soft robotic systems. Even without explicit stiffness measurement, incorporating stiffness-related constraints into the control framework can notably improve performance. This perspective helps explain why general learning-based controllers that do not explicitly account for stiffness modulation may exhibit limited tracking performance, particularly in tasks requiring precision or robustness under varying loads (*52*, *53*).

Furthermore, explicitly accounting for stiffness modulation expands the functional capabilities of antagonistic soft robots beyond simple motion control. When used as a gripper, our strategy enables precise handling of soft and lightweight objects by controlling finger deformation to prevent object tipping or damage. Compared to traditional grippers that rely on direct actuation methods (*54*–*56*), stiffness-aware control allows robots to exploit interaction-induced deviations as informative signals, enabling functions such as object stiffness discrimination alongside manipulation. Related benefits are also demonstrated in liquid pumping against gravity and reconfigurable bridging under varying traffic conditions. More broadly, the importance of stiffness regulation extends beyond the platforms studied here. It is also relevant to emerging antagonistic soft robotic systems, such as untethered robotic fish (*14*–*16*) where the coordination between deformation and stiffness can strongly influence locomotion performance and environmental adaptability (*57*–*59*). For these systems, however, deriving accurate analytical models that explicitly capture stiffness-related behavior is often difficult in practice. Our work provides a practical and rapidly deployable data-driven framework for achieving simultaneous motion control and stiffness regulation while supporting broader exploration of application scenarios and performance boundaries.

Despite the demonstrated effectiveness of the proposed stiffness-driven control strategy, several limitations remain. First, as a data-driven approach learned from finite datasets, the current framework may not fully accommodate parameter variations arising from long-term structural changes in soft robots, such as material aging and wear. Online learning strategies that ensure persistent excitation and effective data selection have the potential to address this limitation by enabling continuous adaptation to evolving system dynamics (*60*, *61*). Second, the present implementation relies on indirect stiffness regulation inferred from actuation inputs and system responses, rather than explicit real-time stiffness sensing, which limits stiffness regulation under rapidly changing interaction conditions. Integrating pressure and visual sensing with multi-sensor fusion offers a promising direction for enabling explicit stiffness estimation and machine learning-based feedback regulation (*62*). In future work, combining online adaptation with multi-sensor feedback may support more autonomous control, allowing antagonistic soft robots to adjust stiffness and motion in response to unstructured environments and task variability.

MATERIALS AND METHODS

Fabrication of the antagonistic robot

The base layer and scales of the scale-inspired layered structure in the antagonistic robot are manufactured using a fused deposition modeling three-dimensional (3D) printer (Raise3D Pro 2) with PLA (Raise3D Premium PLA). To reduce friction, both the base layer and scales are covered with a layer of polytetrafluoroethylene (PTFE) tape that is 0.05-mm thick. The scales are then attached to the base layer using the same PTFE tape.

The assembled layered structure is subsequently placed between two latex films. Silicone glue is used to seal the edges, forming an airtight chamber. An air tube is attached to the chamber to enable the application of negative pressure. This process is repeated to create the opposite side of the antagonistic robot, resulting in a symmetrical structure with two independently controllable chambers. An IMU (JY901S) is placed at the end of the antagonistic robot to measure its bending angle. The design parameters of the antagonistic robots used in different application scenarios are detailed in fig. S10 and table S6.

FE simulations of the antagonistic robot

The FE simulations were conducted using the commercial software ABAQUS Explicit. We used 2D simulations under the plane strain condition. The schematic of the computational model is illustrated in fig. S13A. For all simulations, we utilized four-node bilinear plane strain quadrilateral elements with reduced integration (CPE4R). The mesh used ~7000 elements. Two layers of elements were used in the latex film and the thinnest part of the scale structures to ensure computational accuracy. The base end of the soft robot was fixed with all degrees of freedom constrained. The material parameters used in the simulations are summarized in table S7. To obtain the bending angle θ of the antagonistic robot, each simulation comprised three steps: first, applying gravity; second, applying negative pressure to the chambers; and last, allowing the structure to relax for 1 s.

To validate the FE model, we conducted a series of experiments. The antagonistic soft robot was mounted vertically with its base end fixed. First, we applied varying negative pressures (0 to 80 kPa) to a single chamber of the robot and measured the resulting bending angle θ. Subsequently, we suspended a 30 g of load at the end of the robot, as shown in fig. S13B, and measured the additional deflection angle ($\Delta\theta_F$) caused by this load. Each measurement was repeated five times. We then replicated these experimental conditions in our FE simulations as depicted in fig. S13C. The comparison between experimental and simulation results is summarized in fig. S14. The bending angle θ as a function of the applied negative pressure is shown in fig. S14A, while fig. S14B illustrates the deflection angle $\Delta\theta_F$ caused by the 30 g of load at different negative pressures. In both cases, the simulation results closely replicate the trends observed in the experiments, demonstrating good agreement. This close correspondence validates our FE model and confirms its reliability for further analysis of the robot's behavior.

Following the validation of the FE model, we conducted an additional set of simulations to determine the bending stiffness of the

antagonistic robot. In these simulations, we first replicated the process from our previous simulations to obtain the robot's bending angle θ resulting from the applied negative pressures. However, instead of subsequently applying a vertical load, we applied a moment to the end of the robot and record the induced deflection angle $\Delta\theta_M$, as illustrated in fig. S13D. We chose this approach over the vertical-load method used in the model validation process as it allowed us to measure the bending stiffness of the robot even when it is straight, where the vertical-load method would cause no deflection angle. This moment-based method enabled us to calculate the bending modulus of the robot using the following equation

$$K_b = \frac{M}{\Delta\theta_M} \tag{1}$$

In these calculations, we set the deflection angle $\Delta\theta_M$ to 1°. The results of these simulations are presented in Fig. 1B, providing a comprehensive map of the robot's bending angle and bending stiffness across various pressure combinations in both chambers.

Data collection and model identification

For each robot configuration, the dataset consists of five excitation trials, each lasting 50 s and sampled at 50 Hz, resulting in ~2500 samples per trial and 12,500 samples in total. The excitation inputs are designed to cover representative operating conditions of the antagonistic system, including two unilateral triangular-wave excitation patterns and three coordinated dual-input sinusoidal excitation patterns with different phase offsets. For a single antagonistic robot, each sample contains the bending angle, the two actuator inputs, and the sampling interval. Before the Koopman matrix construction, the recorded state and input variables are normalized.

For the deep Koopman feedforward compensator (DK-FFC), an additional dataset is collected using two trajectories, each lasting 50 s and sampled at 50 Hz. These trajectories are generated by starting from a high antagonistic coactivation level and gradually reducing one actuator input, thereby better capturing the robot's response during large deflections under high-stiffness conditions. The DK-FFC uses a neural network with three hidden layers and is trained offline on a separate computer.

On Raspberry Pi 4B, the offline construction of the Koopman matrices for a single robotic arm requires 39.86 s, and the subsequent derivation of the Koopman model requires 13.27 ms. The DK-FFC training requires 70.60 s on a Windows 10 workstation equipped with an Intel CPU, 31.7-GB RAM, and an NVIDIA GeForce RTX 4060 Laptop GPU. Combined with the 250-s data acquisition time for Koopman model identification and the additional 100-s data acquisition time for DK-FFC training, the total practical time required to obtain a deployable full controller for one robot configuration is approximately 460 s (about 7.67 min). If only the Koopman prediction model is considered, then the corresponding time is ~290 s (about 4.83 min). During online control, the controller is executed at 50 Hz, corresponding to a sampling interval of 20 ms, and the average computation time per control step is 11.61 ms, which is below the sampling interval and compatible with real-time implementation.

Input system

In the antagonistic robot, each chamber is independently controlled by a proportional valve (SMC ITV2090-312 L5). These valves incorporate built-in proportional-integral-differential feedback mechanisms for precise pressure tracking. Specifically, adjusting the input voltage allows for precise positioning of the valve spool, thereby regulating the pressure. A Raspberry Pi is used to generate PWM signals, which are then converted to voltage using a PWM-to-voltage conversion module. Our proposed data-driven control method establishes a direct relationship between the duty cycle of the PWM signal and the bending angle of the robot. This approach bypasses the need for input pre-modeling, eliminating intermediate steps such as modeling the relationship between air pressure and bending angle of the robot or mapping the PWM signal duty cycle to air pressure.

Koopman dynamics

The discrete robot dynamics in the state space manifold $\mathcal{F}$ can be defined as (*38*, *39*, *63*, *64*)

$$\boldsymbol{s}_{k+1} = \boldsymbol{F}(\boldsymbol{s}_k, \boldsymbol{u}_k) \tag{2}$$

where $\boldsymbol{s} \in \mathcal{F}$ is the robot state, $\boldsymbol{u} \in \mathcal{B}$ is the robot input, and $\boldsymbol{F}: \mathcal{F} \times \mathcal{B} \to \mathcal{F}$ is the nonlinear state transition function. Similarly, the Koopman operator $\mathcal{K}$ acting on functions of state space $\mathcal{H}$ is defined by

$$\boldsymbol{\Psi}(\boldsymbol{s}_{k+1}, *) = \mathcal{K}\boldsymbol{\Psi}(\boldsymbol{s}_{k+1}, \boldsymbol{u}_k) \tag{3}$$

where $\Psi: \mathcal{F} \times \mathcal{B} \to \mathcal{H}$ is the lifting function dictionary; $*$ denotes an exogenous input term, typically set to $\boldsymbol{u}_{k+1}$, introduced for formal consistency in the lifted-space formulation rather than being treated as a state variable. Then, the Koopman operator can be obtained by the extended dynamic mode decomposition, yielding a minimum-norm closed-form solution

$$\begin{aligned} \boldsymbol{K} &= \begin{bmatrix} \boldsymbol{A} & \boldsymbol{B} \\ . & . \end{bmatrix} \\ &= \sum_{k=1}^{P-1} \boldsymbol{\Psi}_{k+1} \boldsymbol{\Psi}_k^T \left(\sum_{k=1}^{P-1} \boldsymbol{\Psi}_k \boldsymbol{\Psi}_k^T \right)^{\dagger} \end{aligned} \tag{4}$$

where P represents the number of sampled state-input pairs and † denotes the Moore-Penrose pseudoinverse.

Decoupled bilinear lifting model

The lifting function is designed by

$$\boldsymbol{\Psi} = \left[\underbrace{\boldsymbol{s}_k^T}_{\text{State}} \quad \underbrace{\boldsymbol{\psi}(\boldsymbol{s}_k, \ldots, \boldsymbol{s}_{k-m})}_{\text{Polynomials- based lifting function}} \quad \underbrace{1}_{\text{Constant}} \quad \underbrace{\boldsymbol{s}_k^T \otimes \boldsymbol{u}_{k-1}^T}_{\text{Bilinear lifting function}} \quad \underbrace{\boldsymbol{u}_{k-1}^T}_{\text{Input}} \right]^T \tag{5}$$

where $\boldsymbol{s}_{k\text{-}i}$ denotes past states, $\otimes$ is the Kronecker product, and m represents the number of past states. Considering the dimension of the input $N_{\boldsymbol{u}} = 2n$ and the dimension of the state $N_{\boldsymbol{x}} = n$, the dimensionality of the lifting function is calculated as

$$d(m, n, \nu) = 2n(1+n) + \frac{1}{\nu!} \prod_{i=(1+m)n+1}^{(1+m)n+\nu} i \tag{6}$$

where ν is the highest order of the polynomials $\boldsymbol{\psi}$ and n represents the number of antagonistic robots. In multirobot systems, such as soft grippers, the dimensionality of the lifting function increases exponentially with the number of robot states, affecting the solving speed of embedded systems. Thus, we propose a decoupled bilinear

lifting model for decoupled multirobot systems. This approach first evaluates the Koopman dynamics of each decoupled part. Then, the Koopman dynamics for real-time control can be obtained as

$$\begin{aligned} \boldsymbol{\chi}_{k+1} &= \boldsymbol{A}\boldsymbol{\chi}_k + \boldsymbol{B}\boldsymbol{u}_k \\ \boldsymbol{s}_{k+1} &= \boldsymbol{C}\boldsymbol{\chi}_{k+1} \end{aligned} \tag{7}$$

where $\boldsymbol{\chi}_k = \left[\boldsymbol{\varsigma}_{k,1}^T, \ldots, \boldsymbol{\varsigma}_{k,n}^T\right]^T$, $\boldsymbol{\varsigma}_{k,1} = \left[\boldsymbol{s}_{k,1}^T, \boldsymbol{\Psi}_{k,1}, 1, \boldsymbol{s}_{k,1}^T \otimes \boldsymbol{u}_{k-1,1}^T\right]^T$, $\boldsymbol{A} = \mathrm{diag}(\boldsymbol{A}_1, \ldots, \boldsymbol{A}_n)$, $\boldsymbol{B} = \mathrm{diag}(\boldsymbol{B}_1, \ldots, \boldsymbol{B}_n)$, $\boldsymbol{C} = \mathrm{diag}(\boldsymbol{C}_1, \ldots, \boldsymbol{C}_n)$, and $\boldsymbol{C}_i$ is a row unit vector. Taking $n = m = \nu = 3$ as an example, the dimensionality of the lifting function will decrease from d (3, 3, 3) = 479 to $3d$ (3, 1, 3) = 117, which substantially improves computational scalability for multi-unit systems. It should be noted, however, that this decoupled formulation is intended for modular robotic systems composed of mechanically independent actuation units, where each unit can be treated as an individual subsystem with its own state and input. Therefore, the associated dimensionality reduction is meaningful only when such structural independence exists, as in the gripper and bridge systems studied in this work. By contrast, this formulation is not applicable to intrinsically coupled multi-DOF platforms. For example, in the tendon-driven 2-DOF robot, the yaw and pitch motions are jointly determined by a shared tendon actuation network and must therefore be modeled as a coupled system rather than by the decoupled lifting formulation.

Stiffness-driven solver

The stiffness-driven optimization problem is defined as follows

$$\begin{aligned} \boldsymbol{u}_b &= \underset{\boldsymbol{u}}{\mathrm{argmin}} J\left(\boldsymbol{s}_k, \boldsymbol{u}_k\right) \\ &\text{subject to } \boldsymbol{g}\left(\boldsymbol{s}_k, \boldsymbol{u}_k\right) = 0 \text{ and } \boldsymbol{h}\left(\boldsymbol{s}_k, \boldsymbol{u}_k\right) \le 0 \end{aligned} \tag{8}$$

where $\boldsymbol{g}$ and $\boldsymbol{h}$ contain all equality and inequality constraints, respectively. The cost function within a predictive horizon N_p can be computed via

$$J = \sum_{i=1}^{N_p} \left(\|\boldsymbol{s}_{k+i|k}^e\|_{\boldsymbol{Q}}^2 + \|\Delta \boldsymbol{u}_{k+i-1|k}\|_{\boldsymbol{P}}^2 - \|\boldsymbol{\kappa}\boldsymbol{u}_{k+i-1|k}\|_{\boldsymbol{R}}^2 \right) \tag{9}$$

where $\boldsymbol{s}^e$ represents the state error; $k + i|k$ denotes the prediction of $k + i$ time step at k time step; $\boldsymbol{\kappa} = \boldsymbol{I}_{n\times n} \otimes \boldsymbol{1}_{1\times 2}$; $\|\cdot\|_{\boldsymbol{Q}}^2$ is defined as the $\boldsymbol{Q}$-weighted norm; and $\boldsymbol{Q}$, $\boldsymbol{P}$, and $\boldsymbol{R}$ are related to the weight of variables. The first term on the right-hand side minimizes the state error over the prediction horizon. The second term reduces input variations, while the last term increases the sum of antagonistic inputs to control stiffness. The cost function is solved by MPC (see note S13 for algorithm details). The last term can be improved to enable different stiffness levels as

$$J = \sum_{i=1}^{N_p} \left(\|\boldsymbol{s}_{k+i|k}^e\|_{\boldsymbol{Q}}^2 + \|\Delta \boldsymbol{u}_{k+i-1|k}\|_{\boldsymbol{P}}^2 - \|\boldsymbol{\kappa}\boldsymbol{u}_{k+i-1|k} - \boldsymbol{u}_d\|_{\boldsymbol{R}}^2 \right) \tag{10}$$

where $\boldsymbol{u}_d$ represents the desired input.

Deep Koopman feedforward compensator

To address the slow response of the robot during large deflections, especially in fluidic systems such as the antagonistic robot used in this study, we introduce a deep Koopman feedforward compensator. This approach diverges from the polynomial-based lifting function used in the solver, instead using a neural network with three hidden layers as the lifting function. This choice is motivated by the neural network's superior predictive performance. The increased complexity of the neural network makes it resource-intensive for use in the real-time solver. However, this complexity does not pose substantial issues when used for feedforward operations. In particular, the state-input pairs used to train the neural network are collected by starting with the maximum antagonistic input and then gradually decreasing one side input. Meanwhile, an amplification factor α is used to activate the compensator in the large deflection. The feedforward input $\boldsymbol{u}_f$ can then be calculated as

$$\boldsymbol{u}_f = \alpha \boldsymbol{A}_f \boldsymbol{\Psi}_f\left(\boldsymbol{s}_f\right) \tag{11}$$

where $\boldsymbol{A}_f$ is the trained weight matrix, $\boldsymbol{\Psi}_f$ is the neural network-based lifting function, and $\boldsymbol{s}_f$ is the target state.

PD controller

The PD controller for a single antagonistic soft robot is defined as follows

$$\Delta u = k_p s_k^e + k_d \dot{s}_k^e \tag{12}$$

where $\dot{s}$ denotes the differential of the state, k_p and k_d represent proportional and derivative coefficients. Each chamber of the antagonistic robot is activated separately by using the following law

$$\begin{cases} u_L = u, u_R = 0 & u > 0 \\ u_L = 0, u_R = u & u \le 0 \end{cases} \tag{13}$$

where $u = u + \Delta u$, u_L, and u_R denote the left and right chamber input, respectively. This control law ensures that only one side of the antagonistic soft robot is activated at any given time. Furthermore, two heuristic PD-based controllers with antagonistic stiffening are implemented as comparison baselines. The first strategy is a fixed-input stiffening scheme, defined as

$$\begin{cases} u_L = u_c + u, u_R = u_c & u > 0 \\ u_L = u_c, u_R = u_c + u & u \le 0 \end{cases} \tag{14}$$

where u_c represents the constant input. The second one is a symmetric preload strategy, defined as

$$\begin{cases} u_L = u_s + u \\ u_R = u_s - u \end{cases} \tag{15}$$

where u_s denotes the symmetric preload input. Additional heuristic PD stiffening strategies are described in the note S6.

Perception module

The cost function in the stiffness-driven solver includes a penalty term for input variation, designed to reduce robot chatter. It stabilizes input changes as the robot approaches objects gradually. Moreover, it can be used to determine object contact. As the robot nears an object, the input variation term in the cost function promotes smooth, stable movements. However, upon contact with an object, the robot experiences damping, necessitating larger input variations to maintain its predefined path. This shift in behavior allows us to leverage the input variation as an indicator of object contact. Specifically, we define a contact detection criterion based on the magnitude of input variation

$$\| \Delta u \| > \tau \tag{16}$$

where Δu represents the input variation and $\tau = 0.06\%$ is a predefined threshold value.

Supplementary Materials

The PDF file includes:
Notes S1 to S15
Tables S1 to S8
Figs. S1 to S15
Legends for movies S1 to S4

Other Supplementary Material for this manuscript includes the following:
Movies S1 to S4

REFERENCES

1. W. Dou, G. Zhong, J. Cao, Z. Shi, B. Peng, L. Jiang, Soft robotic manipulators: Designs, actuation, stiffness tuning, and sensing. *Adv. Mater. Technol.* **6**, 2100018 (2021).
2. M. E. Giannaccini, C. Xiang, A. Atyabi, T. Theodoridis, S. Nefti-Meziani, S. Davis, Novel design of a soft lightweight pneumatic continuum robot arm with decoupled variable stiffness and positioning. *Soft Robot.* **5**, 54–70 (2018).
3. Y. Fan, B. Yi, D. Liu, An overview of stiffening approaches for continuum robots. *Robot. Comput. Integr. Manuf.* **90**, 102811 (2024).
4. M. Manti, V. Cacucciolo, M. Cianchetti, Stiffening in soft robotics: A review of the state of the art. *IEEE Robot. Autom. Mag.* **23**, 93–106 (2016).
5. J. Liu, X. Wang, S. Liu, J. Yi, X. Wang, Z. Wang, Vertebraic soft robotic joint design with twisting and antagonism. *IEEE Robot. Autom. Lett.* **7**, 658–665 (2022).
6. W. Gaozhang, Y. Li, J. Shi, Y. Wang, A. Stilli, H. Wurdemann, A novel stiffness-controllable joint using antagonistic actuation principles. *Mech. Mach. Theory* **196**, 105614 (2024).
7. A. D. Marchese, D. Rus, Design, kinematics, and control of a soft spatial fluidic elastomer manipulator. *Int. J. Robot. Res.* **35**, 840–869 (2016).
8. D. H. Kim, Y. Lee, H.-S. Park, Bioinspired high-degrees of freedom soft robotic glove for restoring versatile and comfortable manipulation. *Soft Robot.* **9**, 734–744 (2022).
9. S. Chatterjee, D. Hore, A. Arora, A Security Model to Make Communication Secure in Cluster-Based MANETs, paper presented at the 2017 2nd International Conference on Communication and Electronics Systems, Coimbatore, India, 19 October 2017.
10. N. Takahashi, S. Furuya, H. Koike, Soft exoskeleton glove with human anatomical architecture: Production of dexterous finger movements and skillful piano performance. *IEEE Trans. Haptics* **13**, 679–690 (2020).
11. R. Konda, D. Bombara, S. Swanbeck, J. Zhang, Anthropomorphic twisted string-actuated soft robotic gripper with tendon-based stiffening. *IEEE Trans. Robot.* **39**, 1178–1195 (2023).
12. T. Wang, T. Jin, Q. Zhang, L. Li, G. Wang, Y. Tian, S. Yi, Y. Lin, A bioinspired gripper with sequential motion and mutable posture enabled by antagonistic mechanism. *Adv. Intell. Syst.* **5**, 2200304 (2023).
13. A. H. Memar, E. T. Esfahani, A robot gripper with variable stiffness actuation for enhancing collision safety. *IEEE Trans Ind Electron* **67**, 6607–6616 (2020).
14. Q. Zhong, J. Zhu, F. E. Fish, S. J. Kerr, A. M. Downs, H. Bart-Smith, D. B. Quinn, Tunable stiffness enables fast and efficient swimming in fish-like robots. *Sci. Robot.* **6**, eabe4088 (2021).
15. R. Baines, S. K. Patiballa, J. Booth, L. Ramirez, T. Sipple, A. Garcia, F. Fish, R. Kramer-Bottiglio, Multi-environment robotic transitions through adaptive morphogenesis. *Nature* **610**, 283–289 (2022).
16. S.-D. Gravert, E. Varini, A. Kazemipour, M. Y. Michelis, T. Buchner, R. Hinchet, R. K. Katzschmann, Low-voltage electrohydraulic actuators for untethered robotics. *Sci. Adv.* **10**, eadi9319 (2024).
17. D. Bruder, M. A. Graule, C. B. Teeple, R. J. Wood, Increasing the payload capacity of soft robot arms by localized stiffening. *Sci. Robot.* **8**, eadf9001 (2023).
18. W.-H. Chen, S. Misra, Y. Gao, Y.-J. Lee, D. E. Koditschek, S. Yang, C. R. Sung, A programmably compliant origami mechanism for dynamically dexterous robots. *IEEE Robot. Autom. Lett.* **5**, 2131–2137 (2020).
19. F. Maghooa, A. Stilli, Y. Noh, K. Althoefer, H. A. Wurdemann, Tendon and pressure actuation for a bio-inspired manipulator based on an antagonistic principle, in *2015 IEEE International Conference on Robotics and Automation* (IEEE, 2015).
20. A. D. Marchese, K. Komorowski, C. D. Onal, D. Rus, Design and control of a soft and continuously deformable 2D robotic manipulation system, in *IEEE International Conference on Robotics and Automation* (IEEE, 2014).
21. Y. Toshimitsu, K. W. Wong, T. Buchner, R. Katzschmann, SoPrA: Fabrication & Dynamical Modeling of a Scalable Soft Continuum Robotic Arm with Integrated Proprioceptive Sensing in *2021 IEEE/RSJ International Conference on Intelligent Robots and Systems* (IEEE, 2021).
22. T.-L. Habich, S. Kleinjohann, M. Schappler, Learning-based position and stiffness feedforward control of antagonistic soft pneumatic actuators using gaussian processes, in *2023 IEEE International Conference on Soft Robotics* (IEEE, 2023).
23. C. M. Best, M. T. Gillespie, P. Hyatt, L. Rupert, V. Sherrod, M. D. Killpack, A new soft robot control method: Using model predictive control for a pneumatically actuated humanoid. *IEEE Robot. Autom. Mag.* **23**, 75–84 (2016).
24. M. Trumić, K. Jovanović, A. Fagiolini, Decoupled nonlinear adaptive control of position and stiffness for pneumatic soft robots. *Int. J. Robot. Res.* **40**, 277–295 (2021).
25. M. T. Gillespie, C. M. Best, M. D. Killpack, Simultaneous position and stiffness control for an inflatable soft robot, in *2016 IEEE International Conference on Robotics and Automation* (IEEE, 2016).
26. T. Luong, K. Kim, S. Seo, J. Jeon, C. Park, M. Doh, J. C. Koo, H. R. Choi, H. Moon, Long short term memory model based position-stiffness control of antagonistically driven twisted-coiled polymer actuators using model predictive control. *IEEE Robot. Autom. Lett.* **6**, 4141–4148 (2021).
27. B. Yi, Y. Fan, D. Liu, J. Guadalupe Romero, Simultaneous position-and-stiffness control of underactuated antagonistic tendon-driven continuum robots. *IEEE Trans Autom Sci Eng* **22**, 7238–7254 (2025).
28. M. Trumic, G. Grioli, K. Jovanovic, A. Fagiolini, Force/torque-sensorless joint stiffness estimation in articulated soft robots. *IEEE Robot. Autom. Lett.* **7**, 7036–7043 (2022).
29. J. Wong, E. T. Wilson, N. Malfait, P. L. Gribble, Limb stiffness is modulated with spatial accuracy requirements during movement in the absence of destabilizing forces. *J. Neurophysiol.* **101**, 1542–1549 (2009).
30. Y. Ueyama, E. Miyashita, T. D. Pham, X. Zhou, H. Tanaka, M. Oyama-Higa, X. Jiang, C. Sun, J. Kowalski, X. Jia, Cocontraction of pairs of muscles around joints may improve an accuracy of a reaching movement: A numerical simulation study. *AIP Conf. Proc.* **1371**, 73–82 (2011).
31. P. L. Gribble, L. I. Mullin, N. Cothros, A. Mattar, Role of cocontraction in arm movement accuracy. *J. Neurophysiol.* **89**, 2396–2405 (2003).
32. S. D. Kennedy, A. B. Schwartz, Stiffness as a control factor for object manipulation. *J. Neurophysiol.* **122**, 707–720 (2019).
33. D. W. Franklin, E. Burdet, R. Osu, M. Kawato, T. E. Milner, Functional significance of stiffness in adaptation of multijoint arm movements to stable and unstable dynamics. *Exp. Brain Res.* **151**, 145–157 (2003).
34. M. L. Latash, Muscle coactivation: Definitions, mechanisms, and functions. *J. Neurophysiol.* **120**, 88–104 (2018).
35. B. O. Koopman, Hamiltonian systems and transformation in Hilbert space. *Proc. Natl. Acad. Sci.* **17**, 315–318 (1931).
36. C. W. Rowley, I. Mezić, S. Bagheri, P. Schlatter, D. S. Henningson, Spectral analysis of nonlinear flows. *J. Fluid Mech.* **641**, 115–127 (2009).
37. M. O. Williams, I. G. Kevrekidis, C. W. Rowley, A data-driven approximation of the Koopman operator: Extending dynamic mode decomposition. *J. Nonlinear Sci.* **25**, 1307–1346 (2015).
38. D. A. Haggerty, M. J. Banks, E. Kamenar, A. B. Cao, P. C. Curtis, I. Mezić, E. W. Hawkes, Control of soft robots with inertial dynamics. *Sci. Robot.* **8**, eadd6864 (2023).
39. J. Pan, D. Li, J. Wang, P. Zhang, J. Shao, J. Yu, Autogeneration of mission-oriented robot controllers using Bayesian-based Koopman operator. *IEEE Trans. Robot.* **40**, 903–918 (2024).
40. D. Bruder, X. Fu, R. Vasudevan, Advantages of bilinear Koopman realizations for the modeling and control of systems with unknown dynamics. *IEEE Robot. Autom. Lett.* **6**, 4369–4376 (2021).
41. S. Yu, C. Shen, T. Ersal, Autonomous driving using linear model predictive control with a Koopman operator based bilinear vehicle model. *IFAC Pap.* **55**, 254–259 (2022).
42. P. Foehn, A. Romero, D. Scaramuzza, Time-optimal planning for quadrotor waypoint flight. *Sci. Robot.* **6**, eabh1221 (2021).
43. T. Chen, X. Yang, B. Zhang, J. Li, J. Pan, Y. Wang, Scale-inspired programmable robotic structures with concurrent shape morphing and stiffness variation. *Sci. Robot.* **9**, eadl0307 (2024).
44. C. M. Best, J. P. Wilson, M. D. Killpack, Control of a pneumatically actuated, fully inflatable, fabric-based, humanoid robot, in *2015 IEEE-RAS 15th International Conference on Humanoid Robots* (IEEE, 2015).
45. C. M. Best, L. Rupert, M. D. Killpack, Comparing model-based control methods for simultaneous stiffness and position control of inflatable soft robots. *Int. J. Robot. Res.* **40**, 470–493 (2021).
46. J. Shi, A. Shariati, S.-A. Abad, Y. Liu, J. S. Dai, H. A. Wurdemann, Stiffness modelling and analysis of soft fluidic-driven robots using Lie theory. *Int. J. Robot. Res.* **43**, 354–384 (2024).
47. C. J. Stabile, D. J. Levine, G. M. Iyer, C. Majidi, K. T. Turner, The role of stiffness in versatile robotic grasping. *IEEE Robot. Autom. Lett.* **7**, 4733–4740 (2022).
48. J. Zhu, H. Chen, Z. Chai, H. Ding, Z. Wu, A dual-modal hybrid gripper with wide tunable contact stiffness range and high compliance for adaptive and wide-range grasping objects with diverse fragilities. *Soft Robot.* **11**, 371–381 (2024).

49. A. Firouzeh, J. Paik, Grasp mode and compliance control of an underactuated origami gripper using adjustable stiffness joints. *IEEE/ASME Trans. Mechatron.* **22**, 2165–2173 (2017).
50. J. Shintake, V. Cacucciolo, D. Floreano, H. Shea, Soft robotic grippers. *Adv. Mater.* **30**, 1707035 (2018).
51. Y.-J. Kim, S. Cheng, S. Kim, K. Iagnemma, A stiffness-adjustable hyperredundant manipulator using a variable neutral-line mechanism for minimally invasive surgery. *IEEE Trans. Robot.* **30**, 382–395 (2014).
52. Z. Tang, L. Tian, W. Xin, Q. Wang, D. Rus, C. Laschi, A general soft robotic controller inspired by neuronal structural and plastic synapses that adapts to diverse arms, tasks, and perturbations. *Sci. Adv.* **12**, eaea3712 (2026).
53. M. S. Nazeer, C. Laschi, E. Falotico, RL-based adaptive controller for high precision reaching in a soft robot arm. *IEEE Trans. Robot.* **40**, 2498–2512 (2024).
54. M. Behl, K. Kratz, J. Zotzmann, U. Nöchel, A. Lendlein, Reversible bidirectional shape-memory polymers. *Adv. Mater.* **25**, 4466–4469 (2013).
55. R. Ma, A. Dollar, Yale OpenHand Project: Optimizing open-source hand designs for ease of fabrication and adoption. *IEEE Robot. Autom. Mag.* **24**, 32–40 (2017).
56. C. Tawk, A. Gillett, M. In Het Panhuis, G. M. Spinks, G. Alici, A 3D-printed omni-purpose soft gripper. *IEEE Trans. Robot.* **35**, 1268–1275 (2019).
57. M. J. Mchenry, C. A. Pell, J. H. Long Jr., Mechanical control of swimming speed: Stiffness and axial wave form in undulating fish models. *J. Exp. Biol.* **198**, 2293–2305 (1995).
58. J. H. Long, K. S. Nipper, The importance of body stiffness in undulatory propulsion. *Am. Zool.* **36**, 678–694 (1996).
59. E. D. Tytell, J. A. Carr, N. Danos, C. Wagenbach, C. M. Sullivan, T. Kiemel, N. J. Cowan, M. M. Ankarali, Body stiffness and damping depend sensitively on the timing of muscle activation in lampreys. *Integr. Comp. Biol.* **58**, 861–873 (2018).
60. H. Zhang, C. W. Rowley, E. A. Deem, L. N. Cattafesta, Online dynamic mode decomposition for time-varying systems. *SIAM J. Appl. Dyn. Syst.* **18**, 1586–1609 (2019).
61. X. Huang, W. Zhou, X. Li, L. Zhu, H.-T. Zhang, Online Koopman operator learning to identify cross-coupling effect of piezoelectric tube scanners in atomic force microscopes. *IEEE Trans. Industr. Inform.* **18**, 1111–1120 (2022).
62. J. Lai, B. Lu, H. K. Chu, Variable-stiffness control of a dual-segment soft robot using depth vision. *IEEE/ASME Trans. Mechatron.* **27**, 1034–1045 (2022).
63. D. Bruder, X. Fu, R. B. Gillespie, C. D. Remy, R. Vasudevan, Koopman-based control of a soft continuum manipulator under variable loading conditions. *IEEE Robot. Autom. Lett.* **6**, 6852–6859 (2021).
64. H. Shi, M. Q.-H. Meng, Deep Koopman operator with control for nonlinear systems. *IEEE Robot. Autom. Lett.* **7**, 7700–7707 (2022).

Acknowledgments: We express our appreciation to J. Xiao, K. Wu, and B. Zhang for the support in experiments. **Funding:** Y.W. acknowledges support from the Singapore MOE Tier-2 Award MOE-T2EP50123-0015 and MOE Tier-1 Award RG146/24. **Author contributions:** Conceptualization: J.P., T.C., and Y.W. Methodology: J.P., T.C., J.L., and Y.W. Software: J.P., T.C. Validation: J.P., T.C., and Y.W. Formal analysis: J.P., T.C., J.L., and Y.W. Investigation: J.P., T.C., J.L., and Y.W. Resources: J.P., J.L., and Y.W. Data curation: J.P., T.C. Writing—original draft: J.P., T.C., and Y.W. Writing—review and editing: J.P., T.C., and Y.W. Visualization: J.P., T.C., J.L., and Y.W. Supervision: Y.W. Project administration: J.P. and Y.W. Funding acquisition: Y.W. **Competing interests:** The authors declare that they have no competing interests. **Data, code, and materials availability:** All data and code needed to evaluate and reproduce the results in the paper are present in the paper and/or the Supplementary Materials. This study did not generate any new materials.

Submitted 10 February 2026
Accepted 27 July 2026
Published 2 September 2026
10.1126/sciadv.aeg3346

ScienceAdvances

Muscle coactivation-inspired stiffness-driven control strategy for antagonistic soft robots

Jie Pan, Tianyu Chen, Junwei Li, and Yifan Wang

Sci. Adv. **12** (36), eaeg3346. DOI: 10.1126/sciadv.aeg3346

View the article online
https://www.science.org/doi/10.1126/sciadv.aeg3346
Permissions
https://www.science.org/help/reprints-and-permissions

Use of this article is subject to the Terms of service

Science Advances (ISSN 2375-2548) is published by the American Association for the Advancement of Science. 1200 New York Avenue NW, Washington, DC 20005. The title *Science Advances* is a registered trademark of AAAS.

Copyright © 2026 The Authors, some rights reserved; exclusive licensee American Association for the Advancement of Science. No claim to original U.S. Government Works. Distributed under a Creative Commons Attribution NonCommercial License 4.0 (CC BY-NC).